

Article

The Influence of Texture on the Ductile-to-Brittle Transition Behavior in Fe₂₀Cr_{4.5}Al Oxide Dispersion Strengthened Alloy

Jesus Chao and Carlos Capdevila * 

Centro Nacional de Investigaciones Metalúrgicas (CENIM), Consejo Superior de Investigaciones Científicas (CSIC), Avda. Gregorio del Amo 8, 28040 Madrid, Spain; jchao@cenim.csic.es

* Correspondence: ccm@cenim.csic.es; Tel.: +349-1553-8900

Received: 2 December 2019; Accepted: 25 December 2019; Published: 4 January 2020



Abstract: This paper reports on hardness, tensile properties and notch impact bending toughness values of an Fe₂₀Cr_{4.5}Al oxide dispersion strengthened (ODS) alloy specifically processed to achieved different preferential orientations: random, <100>, <110> and <111> parallel to the bar axis. In spite of the differences in the grain size, it was found for <100>, <111> and random orientations that the mean hardness values on the transverse cross sections is not remarkably sensitive to the texture. On the other hand, a significantly different mean hardness value for the material having the <110> crystalline orientation was found. Regarding the yield strength, it was found for random, <100> and <111> orientations that the yield strength is proportional to the Taylor's factor. The difference between experimental and predicted yield strength values for <110> orientation was attributed to the offset effect induced by the dislocation cell size. The variation of the cleavage fracture strength with the texture was analyzed in the basis of two criteria: one based on the Normal Stress Law (macroscopic nature), and the other based on the assumption that fracture occurs from the propagation of a microcrack-like defect (microscopic nature). In this sense, it was concluded from the fractographic evidences that random and <100> orientations follow a mechanism where the fracture kinks along of the cleavage plane from a penny shaped microcrack nucleated in a second phase particle, meanwhile in the <110> and <111> orientations the fracture propagation arises from a penny shaped defect on the cleavage plane. Finally, the lower shelf values determined for the conditions studied are the same regardless of the texture and microstructure. The effect of texture on the notch toughness was noted where plastic flow predominates, i.e., in the ductile to brittle transition temperature and in the upper shelf energy.

Keywords: texture; mechanical properties; fracture behavior; Fe₂₀Cr_{4.5}Al oxide dispersion strengthened alloy

1. Introduction

It is well known that the mechanical properties of polycrystalline materials can be anisotropic. There are, basically, three factors that can contribute to the anisotropy: morphology and non-uniform distribution of second phase particles, alignment in the microstructure of second phase particles and the preferred crystallographic orientation or texture [1,2]. The alignment of second phase particles in the microstructure is closely linked to the thermomechanical processing and chemical segregation whereas that texture induced anisotropy arises from the directional properties of single crystals, and it is dependent upon the texture intensity of the polycrystalline aggregate, which in turn is related to the thermomechanical processing method [1–3]. In general, no effect of morphology and alignment of second phase particles on yield strength (YS), ultimate tensile strength (UTS) and ductile to brittle

transition temperature (DBTT) has been observed, but reduction in area and absorbed energy at the upper shelf region are strongly dependent of the test direction [1,2,4,5]. It has been observed that upper shelf energy is lowest when the fracture runs parallel to the major axis of the inclusions and presents an inverse correlation with total inclusion projected length per unit area [1,2]; however, such an effect was not observed in the lower shelf region.

The effect of texture on yield strength and UTS can be predicted calculating the Taylor's factor using the method proposed by Hosford and Backofen [6]. The effect of the texture on the ductile-to-brittle transition curve depends on the fracture type involved on each region of the curve:

Cleavage in the lower shelf region. In this region, the effect of texture on the notch toughness is determined by the density and relative orientation regarding to the maximum principal stress of the (100) crystallographic planes since this plane is the cleavage plane [7–11].

Ductile in the upper shelf region. In this region, the effect of texture on notch toughness is determined by the volume fraction and relative orientation regarding to the maximum principal stress of the (110), (123) and (112) planes because these planes are responsible of the plastic deformation of the material [8,11].

Cleavage after notch tip blunting or ductile crack growth in the transition from lower shelf to upper shelf region. In the interval of high temperatures of the lower shelf region, the effect of texture depends on density and orientation of the slip planes upon notch tip blunting and of the cleavage planes upon cleavage fracture. Because the absorbed energy in the upper shelf region is considerably higher than that of the lower shelf region, the effect of texture in the remaining temperatures between lower shelf and upper shelf regions is determined mainly by the density and orientation of the slip planes.

In the present work, the effect of texture on the mechanical properties (hardness, tensile properties at $-196\text{ }^{\circ}\text{C}$ and room temperature (RT) and variation of notch toughness with test temperature in the range from $-196\text{ }^{\circ}\text{C}$ to $400\text{ }^{\circ}\text{C}$) of a Fe20Cr4.5Al oxide dispersion strengthened alloy was analyzed to study the effect of texture on ductile to brittle transition behavior. Analysis of the microstructure to evaluate the role of texture on the fracture surface features by means of optical and scanning electron microscopy was performed.

2. Materials and Methods

The Fe20Cr4.5Al alloy, commercially designed as MA956, was supplied by the Special Metals Corporation (Hereford, UK) in the form of bars. The chemical composition of the alloy is given in Table 1 as determined using X-ray fluorescence spectrometry, wet chemistry and inert gas fusion techniques [12,13].

Table 1. Chemical composition of MA956 alloy (wt. %).

C	Si	Mn	P	S	Cr	Al	Ti	Co	Ni	Cu	O	Y	N	H (ppm)
0.01	0.12	0.10	0.01	0.01	19.30	4.70	0.44	0.07	0.10	0.02	0.11	0.38	0.02	11.00

This body center cubic (BCC) alloy is studied under four different microstructures resulting from specific thermomechanical routes undergone on the original mechanical alloyed powders. Following are these routes and the most relevant microstructural features in each case:

- Hot isostatically pressed at $1050\text{ }^{\circ}\text{C} + 1330\text{ }^{\circ}\text{C}/1\text{ h}$, hereafter denoted "Random". This material supplied as bar of 100 mm diameter presents a ferritic bimodal grain structure consisting of fine equiaxed grains of $2\text{ }\mu\text{m}$ diameter decorating the grain boundaries of large equiaxed grains of $25\text{ }\mu\text{m}$ in diameter [14] (Figure 1a). In this condition, the material presents a random texture with a weak component characterized by a $\langle 100 \rangle$ crystalline direction parallel to the bar axis [14].
- Hot swaged at $1050\text{ }^{\circ}\text{C} + 1330\text{ }^{\circ}\text{C}/1\text{ h}$ bar of 9.5 mm in diameter, hereafter denoted " $\langle 100 \rangle$ ". The resulting microstructure consists of very elongated and coarse grains of $150\text{ }\mu\text{m}$ in diameter

and up to 5103 μm in length with the long axis parallel to the bar axis [14] (Figure 1b). In this condition, a strong η -fiber ($\langle 100 \rangle$ II bar axis) was developed [14].

- Hot extruded at 1050 $^{\circ}\text{C}$ + 1330 $^{\circ}\text{C}/1$ h of 60 mm diameter hereafter denoted as " $\langle 110 \rangle$ ". The microstructure consists of ferritic submicrometric grains elongated in the longitudinal direction of the bar of 1.3 μm length and 0.7 μm in diameter [14] (Figure 1c). This material is characterized by a very strong α -fiber ($\langle 110 \rangle$ II bar axis), [12].
- Recrystallized hot extruded bar of 50 mm diameter in the as-delivered condition from the manufacturer, hereafter denoted " $\langle 111 \rangle$ ". This material presents the most coarse and elongated grains with 3-mm in diameter and of about 20 mm in length, [14] (Figure 1d). Agglomeration of small grains of about 50 μm diameter was also observed [14], which indicates that the recrystallization process has not been completed. In this condition, the 5 to 10 grains that fill up the bar cross section present a $\langle 111 \rangle$ preferential crystalline orientation parallel to the longitudinal direction of the bar [14].

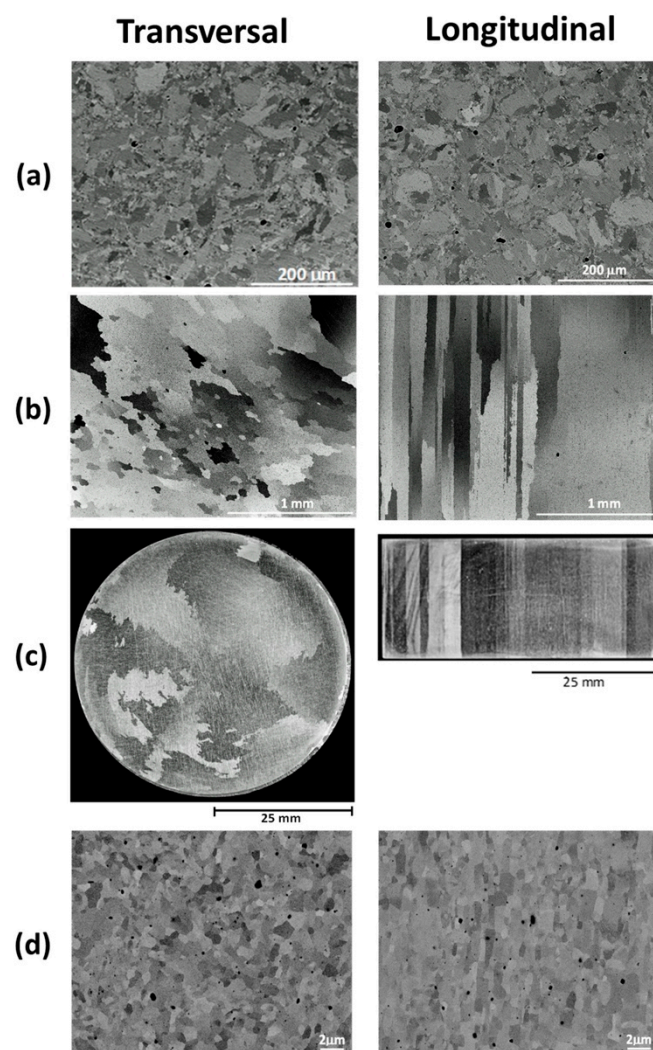


Figure 1. Scanning electron microscopy (SEM) and optical microscope images showing the microstructure of transverse (left) and longitudinal (right) cross sections of: (a) Random, (b) $\langle 100 \rangle$, (c) $\langle 110 \rangle$, (d) $\langle 111 \rangle$ processing conditions.

Two main distribution of mixed (Y,Al) oxide particles uniformly dispersed in the ferritic matrix have been observed [15]: small particles with sizes ranging from 5 nm to 40 nm and large particles up to 500 nm in size [15]. The columnar grains of the microstructure can be attributed to the anisotropic

particle pinning resulting from particle alignment during processing [14]. Moreover, Al₂O₃ particles 100 nm in size and larger, and Ti(C,N) up to a few μm in size were also found [16].

Vickers hardness tests (load 98 N and dwell time 15 s) were carried out at room temperature to measure the macrohardness of the longitudinal and transverse cross sections of the bars in the four conditions. A hardness Vickers manufactured by TecMicro has been used. In the longitudinal cross sections, the indentations were uniformly distributed along of three parallel lines orthogonal to the bar axis in such a way that the diagonals coincide with the longitudinal and transverse directions of the bars. The distance between lines was about 30 mm. In the transverse cross sections, the indentations were carried out so that they and their corresponding diagonals were randomly distributed on the surface. Previous to the hardness test, the surface of the specimens was polished to a 0.05 μm finish in a colloidal silica suspension. For each condition, the hardness values were averaged from at least 40 indentations on each cross section. After the Vickers hardness indentations were complete, Knoop indentations (load 9.8 N and dwell time 15 s) were performed on the same specimens. The goal of the Knoop hardness test was to provide more detail of the effect of texture on hardness as Knoop hardness test is more susceptible to crystalline orientation than Vickers hardness test [17]. Eighteen well-spaced indentations were made in intervals of 10° over a 180° arc on longitudinal and transverse cross sections for which the specimens were previously placed on a turntable. For measurements on the longitudinal cross sections, this interval was the angle between the long diagonal of the indenter and the longitudinal direction of the bar. On the transverse cross section, the interval was between the long diagonal of the indenter and any transverse direction.

The tensile and Charpy specimens were prepared with its longitudinal axis parallel to the bar axis. The round tensile specimens with gage of 4 mm diameter and 30 mm length were tested at $-196\text{ }^{\circ}\text{C}$ and RT using a crosshead speed of 1.2 mm/min. For the purpose of making the results comparable, the dimensions of Charpy specimens (4 mm thickness, 8 mm width, 55 mm length and an U-notch of 2 mm depth and 1 mm notch tip radius) were determined by the smallest diameter of the four bars. The impact tests were conducted on a Wolpert (D6700 model) drop weight impact pendulum of 300 J capacity and a maximum impact velocity of 5.4 m/s. The tests were carried out at temperatures ranging from $-196\text{ }^{\circ}\text{C}$ to $400\text{ }^{\circ}\text{C}$.

The fractographic features of the fracture surface of tensile specimens were examined using an optical microscope and a Jeol JSM6400 scanning electron microscope (Jeol Ltd. 3-1-2 Musashino, Akishima, Tokyo, Japan) operating in 15 kV. The SEM analysis of fracture surfaces were carried out using different magnifications and working distances to determine the macroscopic fracture mode and concurrently characterize the fine details of the fracture surface in order to establish the microscopic mechanism of the fracture initiation.

3. Results

3.1. Main Texture Components

Table 2 lists the maximum orientation distribution function (ODF) intensity of the main texture component for the four different microstructures resulting from specific thermomechanical routes undergone on the original mechanical alloyed materials described in previous sections.

Table 2. Main texture components for the four different microstructures resulting from specific thermomechanical routes undergone.

Condition	I _{max} (ODF)		
	<100>	<110>	<111>
Random	2.1	2.2	1.8
<100>	8.2	0.5	0.8
<110>	1.1	9.1	1.5
<111>	4.2	2.4	7.8

3.2. Hardness Tests

Figure 2 and Table 3 present the mean and standard deviation of the Vickers hardness measurements for longitudinal and transverse cross sections of each material condition. It is observed that the hardness values were homogeneously distributed across the longitudinal and transverse cross sections of the bars. Notwithstanding the relative differences of the grain size to indentation size ($\approx 200 \mu\text{m}$), no remarkable differences between hardness values for $\langle 100 \rangle$, $\langle 111 \rangle$ and Random conditions were found. However, the $\langle 110 \rangle$ condition with the lowest grain size presents the highest hardness. The Vickers hardness data reveal that the alloy is slightly harder in the transverse than in the longitudinal cross section. By contrast, the reverse is true for the Random condition. Vickers hardness indentations showed a slight anisotropic effect in the sense that the indentations were not always square. The two diagonal lengths considered separately present systematic small differences in longitudinal cross sections. Thus, the diagonal length in the transverse direction for the $\langle 110 \rangle$ and $\langle 111 \rangle$ conditions is, respectively, 2.1% and 3% higher than those in the longitudinal direction, whereas for the $\langle 100 \rangle$ condition, the diagonal length in the transverse direction is 1.5% lower than in the longitudinal direction. No systematic differences were observed for the Random condition. The indentation edges in the material in the $\langle 110 \rangle$ condition exhibited slight convexity, whereas in other conditions rectilinear or slightly undulating edges were seen.

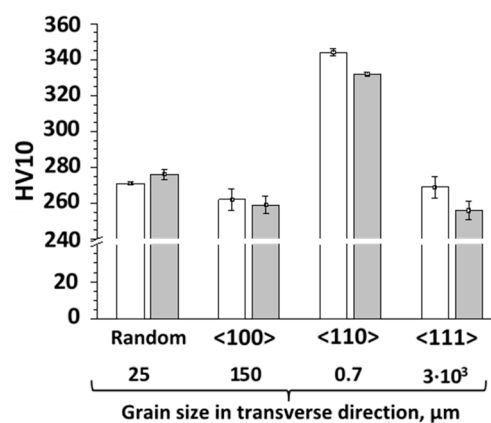


Figure 2. Vickers hardness (10 kgf) numbers of transverse (white columns) and longitudinal (grey columns) cross sections of the four processing conditions.

Table 3. Means and standard deviations of Vickers hardness (HV10) and Knoop hardness numbers, on transverse and longitudinal cross sections of Fe20Cr4.5Al alloy in different conditions.

Condition	Sample Orientation	Grain Size, μm	Vickers Hardness		Knoop Hardness	
			Mean	SD *	Mean	SD *
Random	T	25	271	1	247	37
	L		276	3	247	28
$\langle 100 \rangle$	T	150	262	6	235	29
	L		259	5	245	26
$\langle 110 \rangle$	T	0.7	344	1	317	21
	L		332	1	325	22
$\langle 111 \rangle$	T	3×10^3	269	6	246	37
	L		256	5	247	42

* SD stands for Standard deviation.

For each material condition, the variation in Knoop number with the direction of long diagonal with respect to the longitudinal and transverse directions in the longitudinal and transverse cross sections respectively is shown in Figure 3. Comparatively with the mean of Vickers hardness numbers

in Table 3, the mean of Knoop hardness numbers are slightly lower; however, the Knoop hardness numbers present a higher standard deviation.

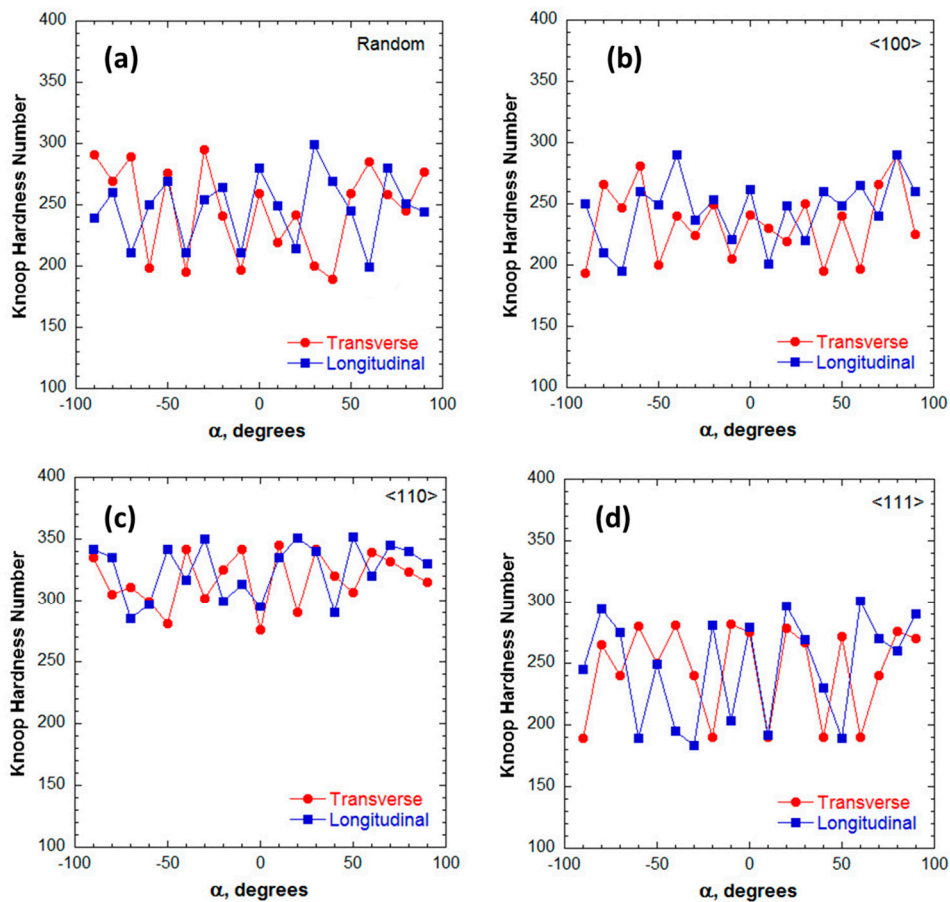


Figure 3. Variation of Knoop hardness (1 kgf) number with indenter orientation for transverse and longitudinal cross sections of the four processing conditions: (a) random, (b) $\langle 100 \rangle$, (c) $\langle 110 \rangle$ and (d) $\langle 111 \rangle$. The value of α is the angle of long diagonal from longitudinal (longitudinal cross section) and arbitrary transverse (transverse cross section) directions.

3.3. Tensile Tests

The nominal stress-strain curves at $-196\text{ }^{\circ}\text{C}$ and RT for all material conditions are shown in Figure 4. The tensile properties: elastic modulus (E), 0.2% yield strength (YS), ultimate tensile strength (UTS), and elongation to failure calculated over a gauge length of 20 mm (ϵ) are listed in Table 4. As can be seen, a very different mechanical response is observed between different conditions, which reflects its strong sensitivity to both the microstructure and the texture of the alloy. It was seen that at $-196\text{ }^{\circ}\text{C}$, the alloy is brittle or shows very low ductility in all conditions except for the case of submicrometric grain size of the $\langle 110 \rangle$ condition in which a plastic elongation as high as 25% is achieved before fracture. This reveals that the DBTT under uniaxial stress conditions for $\langle 110 \rangle$ condition, has not been reached at $-196\text{ }^{\circ}\text{C}$. It is remarkable that for Random, $\langle 100 \rangle$ and $\langle 111 \rangle$ conditions, the brittle fracture occurred just after YS. The elastic region of the curves for the $\langle 100 \rangle$ and $\langle 111 \rangle$ conditions presented several abrupt stress drops which were manifested as audible “clicks” during straining well before YS. The fracture strength is also observed to be dependent of both the microstructure and texture. Thus, the $\langle 100 \rangle$ condition presents the lowest fracture strength (YS = UTS = 1104 MPa) whereas the $\langle 111 \rangle$ condition with the coarsest grain size presents the highest (YS = UTS = 1596 MPa) fracture strength.

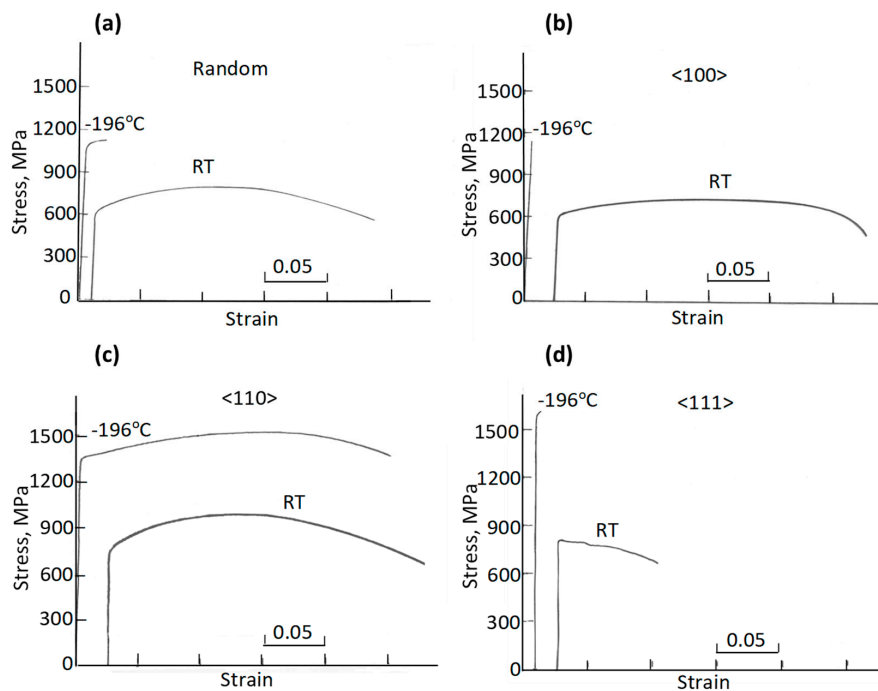


Figure 4. Nominal tensile stress-strain curves at -196°C and room temperature of the four processing conditions: (a) random, (b) $\langle 100 \rangle$, (c) $\langle 110 \rangle$ and (d) $\langle 111 \rangle$.

Table 4. Results of tensile and bending impact tests of Fe20Cr4.5Al alloy in different conditions.

Condition	Tensile Properties					Taylor's Factor	Impact Bending		
	T/ $^{\circ}\text{C}$	E/GPa	YS/MPa	UTS/MPa	$\epsilon/\%$		LSE/J	USE/J	DBTT/ $^{\circ}\text{C}$
Random	20	200	648	804	8.7	2.7	2	24	-20
	-196		1100	1160	3.0				
$\langle 100 \rangle$	20	160	636	732	26.2	2.4	2	42	8
	-196		1104	1104	0				
$\langle 110 \rangle$	20	185	790	970	25.8	2.5	2	35	-70
	-196		1290	1455	25.2				
$\langle 111 \rangle$	20	290	810	816	7.8	3.2	2	33	-40
	-196		1596	1596	0				

E—Young modulus; YS—Yield strength; UTS—Ultimate tensile strength; ϵ —Elongation to failure; LSE—Lower shelf energy; USE—Upper shelf energy; DBTT—Ductile to brittle transition temperature.

Young's modulus at room temperature is maximum ($E = 290$ GPa) for $\langle 111 \rangle$ condition and minimum ($E = 160$ GPa) for $\langle 100 \rangle$ condition which is in agreement with those reported for monocrystals of Fe19Cr alloy tested at RT at the same crystallographic directions [16]. However, the Young's modulus for $\langle 110 \rangle$ condition ($E = 185$ GPa) is lower than that tested in $\langle 110 \rangle$ direction of Fe19Cr alloy [18]. For Random condition a similar value ($E = 200$ GPa) to that of polycrystals of Fe19Cr was found [18].

The tensile response at RT shows ductile behavior for the four conditions. Meanwhile, the Random, $\langle 100 \rangle$ and $\langle 110 \rangle$ conditions exhibit continuous yielding and the $\langle 111 \rangle$ condition presents an initial round yield drop followed by deformation at a continuously decreasing applied stress to final fracture. At RT, the YS and the UTS are also observed to be strongly dependent of the microstructure and texture of the material. The $\langle 100 \rangle$ condition presents the lowest YS (YS = 636 MPa) and UTS (732 MPa) values, whereas the $\langle 111 \rangle$ condition presents the highest YS (YS = 810 MPa) and an UTS value of 816 MPa, almost identical to YS. The $\langle 110 \rangle$ condition presents a similar YS to that of the $\langle 111 \rangle$ condition, in spite of the enormous difference in the grain size, whereas the UTS = 970 MPa value is the largest of all. On the other hand, the $\langle 111 \rangle$ condition presents the lowest elongation to failure (ϵ) and the

$\langle 100 \rangle$ and $\langle 110 \rangle$ the highest. It should be borne in mind, however, that for the $\langle 111 \rangle$ condition, the deformation was not uniformly distributed on the full gage length, but it was only concentrated in the first region of yielding in which necking and later stage of fracture take place.

Fractographic Analysis of Fracture Surface of Tensile Specimens

Figure 5a shows the fracture surface of the material in the Random condition at $-196\text{ }^{\circ}\text{C}$. The macroscopic view (Figure 5a-left) shows a flat fracture surface perpendicular to the tensile axis in which the initiation point of the fracture is appreciated. Detailed view of the initiation zone of the fracture is shown in Figure 5a-right. It is seen from the flat facets, small in size, that cleavage transgranular occurred. It can be also observed that the microstructural feature controlling the fracture initiation consists of a group of small pores (Figure 5a-right). However, the initiation point is not a pore itself, but in the matrix between pores, presumably due to the increase of pore-induced stress triaxiality. The fracture surface of the alloy in the $\langle 100 \rangle$ condition at $-196\text{ }^{\circ}\text{C}$ is shown in the SEM micrographs of Figure 5b. As for the Random condition, a flat fracture surface, which occurs by transgranular cleavage, is observed in Figure 5b. As can be observed more in detail in Figure 5b-left, the fracture propagates from a penny shaped crack nucleated in a second phase particle. Figure 5c presents SEM micrographs showing the fracture surface of the alloy in the $\langle 110 \rangle$ condition at $-196\text{ }^{\circ}\text{C}$. In Figure 5c-left, it is observed that fracture occurs in a plane orthogonal to the tensile axis in which a fracture initiation zone can be observed near the specimen center. In progressive higher magnifications no microstructural features controlling the fracture initiation were found (Figure 5c-right). Because fracture of tensile specimen occurred after considerable reduction of area in transverse cross section, it is assumed that the fracture initiation is controlled by the stress triaxiality state, which is maximum at the center of cross section. Finally, it is remarked that the fracture micromechanism for this condition was not by cleavage but by quasi-cleavage (Figure 5c-right).

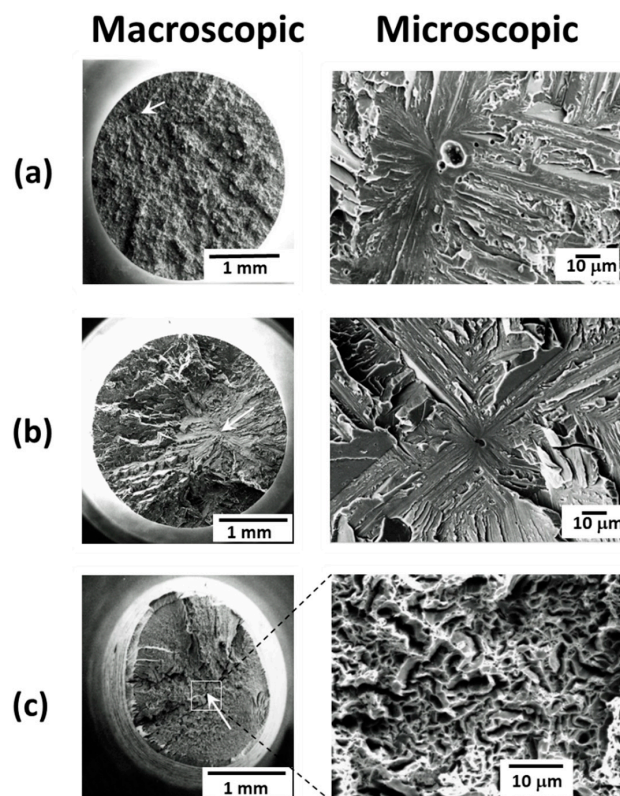


Figure 5. Macroscopic (left) and microscopic (right) SEM images of the fracture surface of tensile specimens tested at $-196\text{ }^{\circ}\text{C}$ of: (a) Random, (b) $\langle 100 \rangle$ and (c) $\langle 110 \rangle$ processing conditions. White arrows indicate the fracture initiation zone.

The different details of the fracture surface of the alloy in the $\langle 111 \rangle$ condition at $-196\text{ }^{\circ}\text{C}$ are shown in the micrographs of Figure 6. Figure 6a is a macroscopic view showing the fracture initiates near specimen surface and the staggered nature of the crack propagation through the transverse cross section of the specimen. Observations in progressively higher magnifications reveal no microstructural features controlling the fracture initiation (Figure 6b). Apparently, it is seen that the fracture initiation takes place at the intersection of three cleavage planes (Figure 6a,b). Figure 6c is an optical macrograph showing the fracture profile, indicating an inclination angle of about $35\text{--}40^{\circ}$ between fracture facets and the tensile axis. In spite of the facets inclination, the average plane of the fracture runs normal to the tensile axis.

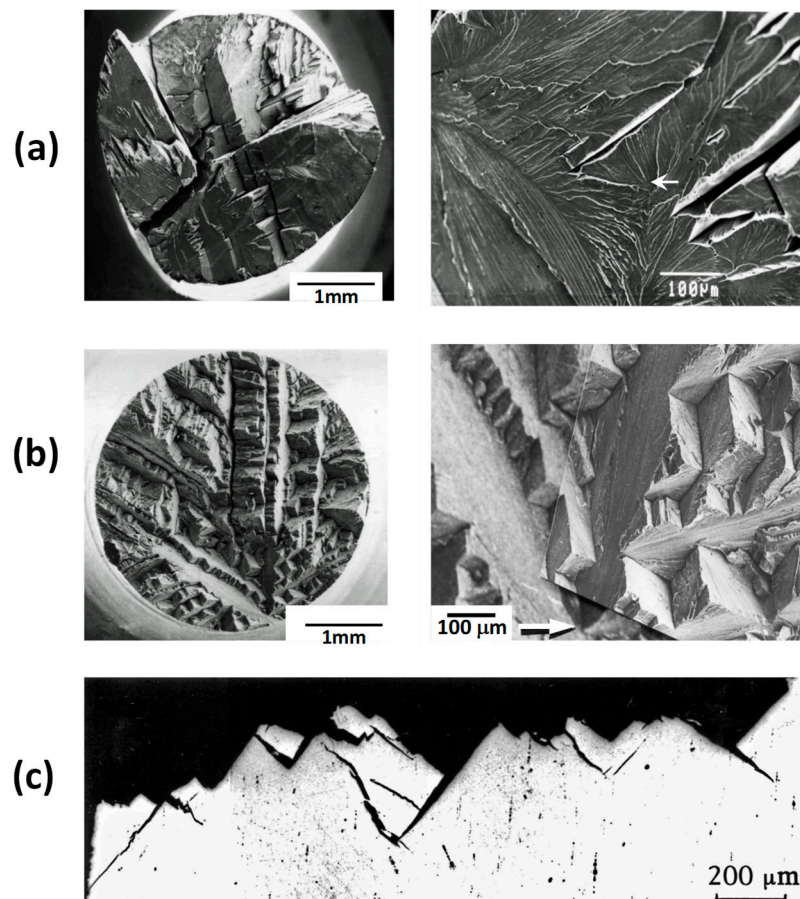


Figure 6. Macroscopic (left) and microscopic (right) SEM views of fracture surface of tensile specimen tested at (a) room temperature and (b) tensile specimen tested at $-196\text{ }^{\circ}\text{C}$. (c) Optical microscope image showing a lateral view of fracture surface of tensile specimen tested at $-196\text{ }^{\circ}\text{C}$. White arrows indicate the initiation fracture zone.

The fracture surfaces of tensile specimens tested at RT of the material in Random, $\langle 100 \rangle$ and $\langle 110 \rangle$ conditions was characterized by microvoid coalescence followed by localized shear, whereas that of the alloy in $\langle 111 \rangle$ condition occurred by cleavage after of marked reduction of area.

3.4. Charpy Tests

Figure 7 shows the impact absorbed energy plotted as a function of test temperature for each of the four material conditions. The lower and upper shelf energies, LSE and USE, respectively, and the ductile to brittle transition temperature DBTT, which corresponds to the average value of LSE and USE values, are listed in Table 3. All four conditions exhibit the same LSE, i.e., the LSE is apparently insensitive to both the grain size and the texture (Figure 7 and Table 3). The $\langle 100 \rangle$ condition presents

the highest USE (USE = 42 J), a rapid transition to LSE and, the highest DBTT (DBTT = 8°). The <111> and <110> conditions, with the highest and lowest grain size, respectively, display comparable USE but significant differences in both the DBTT (−40 °C and −70 °C, respectively) and transition rates from upper to lower shelf regions. Although part of the difference in DBTT for these conditions could be attributed to the difference in the grain size, another important contribution would be due to the texture. On the other hand, the difference in DBTT of the material in <100> (DBTT = +8 °C) and <111> (DBTT = −40 °C) conditions is due mainly to the differences in texture. The Random condition presents the lowest USE and a DBTT = −20 °C.

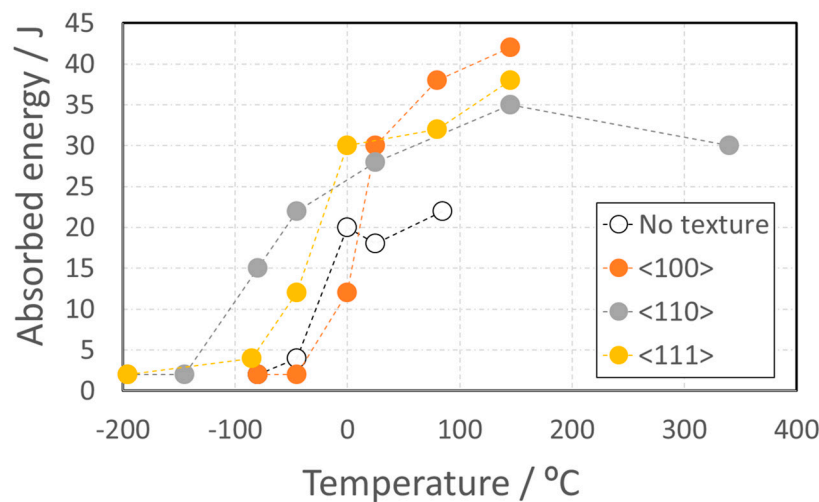


Figure 7. Ductile-brittle transition curves obtained from Charpy impact tests of Random, <100>, <111> and <110> processing conditions.

Fractographic Analysis of Fracture Surface of Charpy Specimens

The experimental results of previous investigations suggest no clear differences in the microstructural features controlling the initiation of the cleavage fracture for the four material conditions [19]. Thus, for test temperatures well into the lower shelf region, and disregarding the material condition, it was reported that cleavage fracture initiated at second phase particles, at the matrix between small pores or at the notch tip [19]. In contrast to what occurs in the DBT region, the weak link model is in general not applicable well into the LS region, because various initiation points determine the cleavage failure. The fracture surface of specimens tested at +150 °C temperature for any material condition presents morphologic features typically ductile of microvoid coalescence; however, the microvoid density of the fracture surface of the Random condition specimens is significantly higher than in other material conditions, which is consistent with its lower value of USE.

4. Discussion

4.1. Hardness

Two factors could influence in the Vickers hardness numbers of the transverse cross sections of the bars, the grain size and the texture. Early investigation has shown that the average hardness number of single crystals of silicon ferrite indented in (001), (110) and (111) planes ranges between 206–208, and then, it was considered that the hardness is independent of the indented plane [20]. Regarding our study, and in spite of the great differences in the grain size for the <100>, <111> and Random conditions, no remarkable differences in hardness were found (Figure 3 and Table 2). Therefore, it might be concluded from this study that hardness is independent of texture. Considering that for the <100> and Random conditions the indentation size ($\approx 200 \mu\text{m}$) was considerably higher than the grain size, and the hardness is independent of the texture, it would also be likely that the hardness is not remarkably influenced by the grain size. It is therefore suggested, in agreement with previous

work [21], that the higher hardness number of the material in the <110> condition is due to the higher dislocation density in the form of dislocation cells.

The scatter in Knoop hardness values that was observed in this study (Figure 4 and Table 2) may be related to the hardness anisotropy that occurs in many materials. For example, in silicon ferrite single crystals, Knoop numbers vary from 180 to 240 as a function of the crystallographic orientation of the long diagonal of indenter [20], and to a lesser extension of the crystallographic plane indented [20]. In polycrystalline ferritic materials, hardness anisotropy of crystallographic origin could be expected if the material is strongly textured. Although the variation range of Knoop hardness of transverse cross sections of the studied alloy is comparable to that observed in silicon ferrite crystals, no cyclic variation in Knoop hardness with orientation of long diagonal was observed, which could be attributed, in part, to the heterogeneous distribution of yttria dispersoids and, in part, to the polycrystalline nature of the alloy.

4.2. Tensile Tests

It is well known that when a crystal is stressed, slip begins when the shear stress on some slip system reaches a critical value τ_c [22]. The Schmidt's law describes the relationship between the applied stress, σ , and the resolved shear stress, τ , using slip plane normal direction and slip direction according the following equation [22]:

$$\tau = m\sigma = \sigma \cos \phi \cos \lambda \quad (1)$$

where m is the Schmidt's factor and ϕ and λ are the angles between the applied stress direction and the slip direction and the slip plane normal direction respectively. Assuming the critical shear stress is independent of the orientation, the value of the applied stress, σ , for a particular condition where the shear stress, τ reaches the critical value, τ_c , might be determined by the reciprocate of m factor. The deformation mechanisms in the grains of a polycrystal are similar as those in a single crystal, but compatibility requirement of deformation between neighboring grains must be achieved [23]. According to Taylor's analysis, the flow behavior of a polycrystal under uniaxial tension can be calculated as [23]:

$$\sigma = M\tau \quad (2)$$

$$d\varepsilon = \frac{d\gamma}{M} \quad (3)$$

where $d\gamma$ is the incremental slip on the individual slip systems, $d\varepsilon$ is the incremental axial strain and M is the Taylor's factor, which depends on the crystalline orientation. Thus, the yield strength of strongly textured metallic materials also depends of the preferential orientation of the grains to direction of applied stress. The slip systems with minimum M-factor will be most favored to slip under uniaxial stress. Earlier investigations have demonstrated that ferritic body-centered-cubic materials deform by <111> pencil glide on any plane ((110), (123) and (112)) containing a <111> direction [21]. For this glide system, Table 3 shows the Taylor's factor for Random, <100>, <110> and <111> orientations [23,24]. For instance, taking the yield strength for <100> orientation and using the appropriate M-factor it can be estimated for any other orientation, x , the yield strength using the following expression:

$$\sigma_{\langle x \rangle} = \frac{M_{\langle x \rangle}}{M_{\langle 100 \rangle}} \sigma_{\langle 100 \rangle} \quad (4)$$

It can be seen that Equation (4) gives reasonable predictions except for <110> orientation in which a remarkable difference of 150 MPa between predicted and experimental values appears. It is suggested that this difference could be attributed to the difference in dislocation density in the form of submicrometric dislocation cells in the material. It is also noteworthy that the hardening associated to the difference in dislocation density is similar to that of the hardening texture induced in the material with <111> orientation, which presents the maximum value of Taylor's factor regarding to those

of all possible orientations [23]. Because of the Taylor's factor is maximum for <111> orientation, once yielding begins, the Taylor's factor decreases, and then, geometrical softening occurs [25]. The softening may be so severe that deformation is concentrated in the firsts regions of yielding, and induces severe necking and subsequent fracture in these regions [25].

There are a lot of publications in the literature concerning with the correlation of yield strength and hardness [26–29]; however, to the author's knowledge, the effect of texture in strongly textured materials on the relationship between hardness and yield strength has not been addressed yet. First, it must be remarked that yield strength and hardness are different mechanical properties, although good correlations and some theoretical basis has been established [30]. Earlier investigations have shown for Fe–Si monocrystals that hardness is independent of the crystallographic plane indented [20]. However, the yield strength is strongly dependent of the tensile direction [25]. For the alloy studied here, similar results to those found for Fe–Si monocrystals has been observed as described in previous sections. Using the following relationship between yield strength and hardness proposed in [31]:

$$YS = 3.28 \times HV - 221 \quad (5)$$

and the hardness values in Table 2, it can be seen that accurate predictions of the yield strength can be obtained for the analyzed conditions except for <111> conditions. Therefore, no general relationship can be established without taking into account the strain hardening of the material [21] or the texture.

The differences found among fracture strength at $-196\text{ }^{\circ}\text{C}$ for the different material conditions can be attributed to the different textures and microstructures developed in each case. To analyze the fracture strength data, the Normal Stress Law established for Shoncke for sodium chloride crystals [32], and extended to the fracture strength of metallic crystals with different lattice structure [22], has been adopted as the starting point. According to this law, a crystal breaks when a critical normal stress (k) is reached on the cleavage plane:

$$\sigma_f \cos^2 \lambda = k \quad (6)$$

where λ is the angle between the normal direction of the cleavage plane and the tensile stress direction and σ_f is the applied stress at fracture. Since cleavage fracture takes place along the specific (100) crystallographic planes, different σ_f values are obtained for different orientations (λ -angles) of the cleavage plane, taking the fracture strength value at $-196\text{ }^{\circ}\text{C}$ as 1100 MPa for the <100> condition ($\lambda = 0^{\circ}$) as a reference value. Table 5 shows the calculated values for any other material condition according with Equation (6). It can be seen that the calculated values are considerably higher than those obtained from experimental test, and thus, the Normal Stress Law does not work for the present alloy.

Table 5. Experimental and predicted values of the fracture strength of tensile specimens tested at $-196\text{ }^{\circ}\text{C}$ of Fe20Cr4.5Al in different conditions.

Condition	α , degrees	β , degrees	Experimental		Predicted	
			σ_F /MPa	σ_N /MPa	σ_{fK} /MPa	σ_{fS} /MPa
Random	-	-	1160	-	1230	1230
<100>	0	0	1104	1104	1104	1104
<110>	45	45	1610 (*)	2208	1388	1531
<111>	55	35	1596	3356	1886	2230

α —deflection angle of the kink with the main crack or angle between normal direction to cleavage plane and tensile direction; β —angle between tensile direction and cleavage plane; σ_F —experimental fracture strength; σ_N —fracture strength estimated from Sohncke's Normal Law, Equation (6); σ_{fK} —fracture strength of kinked penny shaped crack, Equation (15); σ_{fS} —fracture strength of slanted penny shaped crack, Equation (18). *—True maximum fracture stress after 25.2% elongation. It is remarked that in this condition, the fracture occurred by quasi-cleavage.

The tensile curves in Figure 4 and the fractographic analysis reveal that the fracture of tensile specimens tested at $-196\text{ }^{\circ}\text{C}$ develops from the propagation of a microcrack-like defect after the onset of yielding. It is generally accepted that the process of cleavage fracture can be attributed to the

nucleation of a microcrack followed by its dynamic propagation across the surrounding matrix [33–35]. This requires that the local stress must exceed a certain critical value [33–35]. According to Griffith's theory, a microcrack in a solid would become shelf-propagating when the energy release rate, G , became at least equal than the rate of increase of surface energy γ_s of the extending microcrack [36]:

$$G \geq 2\gamma_s \quad (7)$$

Using the terminology of Linear Elastic Fracture Mechanics, the energy release rate may be expressed as follows [37]:

$$G = \frac{K_{eff}^2(1-\nu^2)}{E} \quad (8)$$

$$K_{eff} = K_I^2 + K_{II}^2 \quad (9)$$

where K_{eff} , K_I and K_{II} are the effective, mode I fracture and mode II fracture stress intensity factors, respectively, and E and ν are the Young's modulus and the Poisson's ratio. Two microcracking types were considered to estimate the fracture strength as a function of the material condition, kinked penny shaped microcrack and slanted penny shaped microcrack.

Kinked penny shaped microcrack. It is supposed that a microcrack is nucleated in a second phase particle so that it is normal to the tensile direction and then incipiently propagates along the cleavage plane of the matrix (Figure 8a).

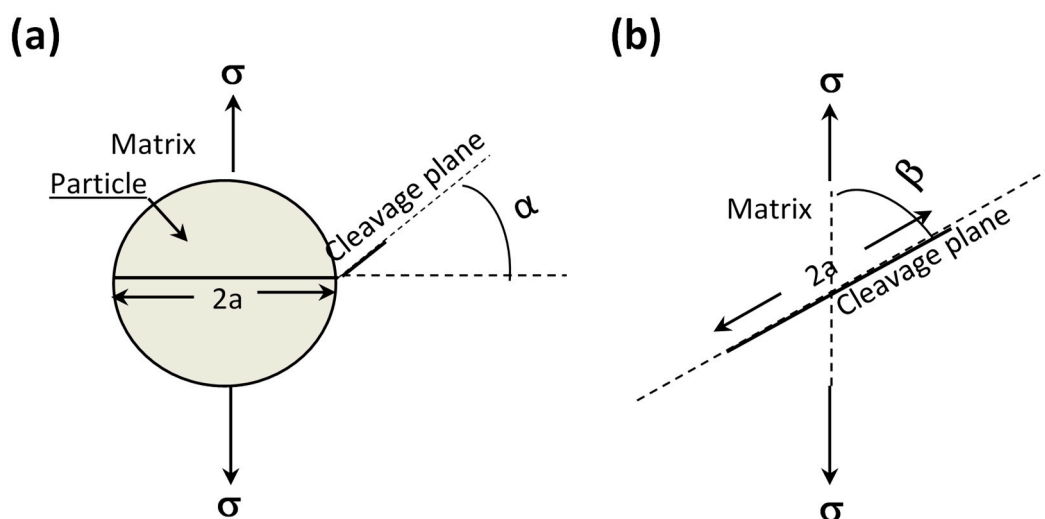


Figure 8. Scheme of the cracking models used to estimate the cleavage fracture strength: (a) kinked penny shaped cracking and (b) slanted penny shaped cracking.

The mode I stress intensity factor, K_I , near the end of a penny shaped crack of a half-crack length, subjected to tensile stress, σ , at infinity is [38]:

$$K = \frac{2}{\pi} \sigma \sqrt{\pi a} \quad (10)$$

For a penny shaped microcrack of a half-crack length, the mode I and mode II stress intensity factors $k_I(\alpha)$ and $k_{II}(\alpha)$ near the end of an infinitesimal kinked crack can be expressed as a function of Equation (10) as follows [39,40]:

$$k_I(\alpha) = C_{11}(\alpha)K_I \quad (11)$$

$$k_{II}(\alpha) = C_{21}(\alpha)K_I \quad (12)$$

In which:

$$C_{11}(\alpha) = \frac{1}{4} \left(3 \cos \frac{\alpha}{2} + \cos \frac{3\alpha}{2} \right) \quad (13)$$

$$C_{21}(\alpha) = \frac{1}{4} \left(\sin \frac{\alpha}{2} + \sin \frac{3\alpha}{2} \right) \quad (14)$$

where α is the deflection angle of the kink with the main microcrack. Substituting (11)–(12) into Equation (8) and the result in Equation (7), it is found that the stress, σ_{fk} , necessary to kinking a penny shaped crack along of cleavage plane is:

$$\sigma_{fk} = \left\{ \frac{\pi E \gamma}{2\alpha(1-\nu^2)(C_{11}^2(\alpha) + C_{21}^2(\alpha))} \right\}^{1/2} \quad (15)$$

Taking σ_{fk} as the fracture strength value of the material in the $\langle 100 \rangle$ condition (1100 MPa), $\alpha = 0$, $a = 5 \times 10^{-4}$ mm, $E = 170$ GPa and $\nu = 0.3$ as input data into Equation (15), the surface energy γ is calculated to be 2.2 J/m^2 , which is consistent with the one reported by Hann for Fe-single crystal [33]. Substituting now the above values of $\gamma = 2.2 \text{ J m}^{-2}$, $a = 5 \times 10^{-4}$ mm, $\nu = 0.3$, and the corresponding values of E and α into Equation (15), the σ_{fk} values listed in Table 4 are obtained.

Slanted penny shaped crack. It is supposed that a crack nucleates in a defect of the crystal lattice of the matrix and immediately propagates along the cleavage plane (Figure 8b).

In this case, the mode I and mode II fracture near the end of a β -slanted penny shaped crack of a half-crack length placed on the cleavage plane undergone to tensile stress, σ , at infinity, are [37]:

$$K_I = \frac{2}{\pi} (\sigma \sin^2 \beta) \sqrt{\pi a} \quad (16)$$

$$K_{II} = \frac{4}{\pi(2-\nu)} (\sigma \sin \beta \cos \beta) \sqrt{\pi a} \quad (17)$$

where β is the angle between tensile direction and the cleavage plane. Substituting Equations (16)–(17) into Equation (8) and the result in Equation (7), it is found that the stress, σ_{fs} , necessary to propagate a slanted penny shaped crack along of a cleavage plane can be calculated from the following equation:

$$\sigma_{fs} = \frac{\left\{ \frac{\pi \gamma E}{2a(1-\nu^2)} \right\}^{1/2}}{\sin \beta \left[1 + \cos^2 \beta \frac{(4-\nu)\nu}{(2-\nu)^2} \right]^{1/2}} \quad (18)$$

Similar calculations to those of kinked penny shaped crack were performed, and these results are also listed in Table 5.

For the σ_{fk} calculation, it was assumed that for the Random (No texture) condition, there was no crack kinking ($\alpha = 0^\circ$) or $\beta = 90^\circ$. It is evident in this condition that those grains with $\langle 100 \rangle$ crystalline direction parallel to tensile direction will determine the cleavage failure of tensile specimen. Accordingly, the experimental cleavage strength values of Random and $\langle 100 \rangle$ conditions are similar.

Comparing σ_{fk} and σ_{fs} values with the experimental σ_F result for $\langle 111 \rangle$ condition, it is observed that the crack kinking model predicts the experimental result more accurately. It make no sense to compare the predictions of the models with the experimental result for $\langle 110 \rangle$ conditions, because in this condition, fracture occurred by quasi-cleavage instead of full cleavage. We think the cleavage fracture strength value is near to YS at -196°C (1290 MPa), because cleavage fracture occurred once a little bit of plastic deformation has developed. Such a value would be more in line with that predicted by the kinking crack model than with that predicted by the slanted crack model.

4.3. Charpy Tests

The influence of texture on the variation with temperature of notch toughness (ductile to brittle transition temperature) was considered for cleavage (lower shelf region), mixed ductile-cleavage (transition region) and ductile (upper shelf region) fracture modes. The LSE depends on the orientation to maximum principal stress direction and density of (100) planes, since these planes are the only crystallographic planes in which cleavage can occur [7–11]. The above results of notch toughness at the LS region have shown the LSE values are the same disregarding of condition (microstructure and texture) of material. However, taking into account the orientation of the cleavage planes (100) regarding to the bar axis for the different material conditions, it could be expected, if propagation is the controlling step for cleavage, that the LSE value varies according to the following inequality:

$$LSE_{\langle 111 \rangle}(35^\circ) > LSE_{\langle 110 \rangle}(45^\circ) > LSE_{\langle \text{Random} \rangle} \geq LSE_{\langle 100 \rangle}(0^\circ) \quad (19)$$

Two possible reasons could to explain the experimental results. First, the step for cleavage fracture is a crack-nucleation instead of crack-propagation controlled mechanism. Because the morphology and distribution of second phase is similar for all conditions, it could be expected that the LSE value were the same for all material conditions. Second, the Charpy test method was not sensitive enough to discern the implicit differences in the inequality (19).

In the upper shelf region, ductile fracture by nucleation and coalescence of microvoids is accompanied of severe plastic deformation. Ferritic steels deform by “pencil” glide on any (110), (123) and (112) planes at $\langle 111 \rangle$ direction [23]; however, as (110) is densely packed, it could be argued that deformation occurred more easily on (110) plane and then that the absorbed energy in the impact test can be higher than when the material deforms on (112) and/or (123) slip planes [41,42]. Moreover, following in the same argument, it can be also argued the absorbed energy could be even larger when the (110) plane is subjected to the maximum shear stress which occurs when this plane is inclined 45° regarding to the direction of the maximum principal stress, i.e., when maximum principal stress acts parallel to the $\langle 100 \rangle$ direction. Based on these considerations, it could therefore be concluded that the material in the $\langle 100 \rangle$ condition should present the highest USE value, which is in accordance with the above experimental results.

In the cleavage to ductile transition region, cleavage is preceded of notch tip blunting in the interval of low temperatures of transition region near the LS region, while in higher temperatures before the US region, cleavage is preceded by notch tip blunting followed by ductile crack growth. An increase in volume fraction of the {110} on an inclined plane 45° regarding to direction of the maximum principal stress ($\langle 100 \rangle$ parallel to maximum principal stress) would facilitate the development of notch tip blunting. This would make it more difficult to cause cleavage because stress concentration ahead of notch tip decreases although crack nucleation and strain hardening would be facilitated. With this in mind, it seems complex to predict the effect of texture on DBTT; however, it is possible to estimate a lower DBTT limit, at least qualitatively, as the temperature in which LS begins. Having into account the variation of yield strength with temperature (Table 4) and the cleavage fracture strength (Table 4) for the different material conditions it is proposed the temperature in which LS begins would vary according to the following inequality:

$$T_{\langle 111 \rangle} < T_{\langle 110 \rangle} < T_{\langle \text{Random} \rangle} \leq T_{\langle 100 \rangle} \quad (20)$$

The DBTTs of the material in the different conditions showed in Table 3 are agreement with this inequality except for $\langle 111 \rangle$ and $\langle 110 \rangle$ that occupy exchanged positions. Therefore, the dislocation cells in the $\langle 110 \rangle$ condition cause a notable reduction of DBTT.

5. Conclusions

The influence of texture on hardness, tensile properties and notch impact bending toughness on a Fe₂₀Cr_{4.5}Al ODS alloy processed to achieved random, <100>, <110> and <111> preferential orientations has been studied in this work. The following conclusion has been raised:

1. Tensile curves and fractographic analysis reveal that the fracture of tensile specimens tested at −196 °C develops from the propagation of a microcrack-like defect after the onset of yielding.
2. Two criteria to determine the cleavage mechanism have been analyzed. One of macroscopic nature, based on the Normal Stress Law, and the other of microscopic nature, which assumes that fracture occurs from the propagation of a microcrack-like defect. The results show that the applied tensile stress for cleavage fracture is considerably over-predicted with the Normal Stress Law while the second criterion gives accurate predictions.
3. The effect of texture on the cleavage strength of tensile specimens can be properly predicted with the kinking crack model.
4. The lower shelf values determined for the conditions studied are the same regardless of the texture and microstructure. The effect of texture on the notch toughness was noted where plastic flow predominates, i.e., in the ductile to brittle transition temperature and in the upper shelf energy.

Author Contributions: Both authors were involved in the results discussion and in finalizing the manuscript. All authors have read and agreed to the published version of the manuscript.

Funding: This research received funding from the Spanish Ministerio de Ciencia, Innovación y Universidades in the form of a Coordinate Project (MAT2016-80875-C3-1-R). The authors would like to acknowledge financial support from the Comunidad de Madrid through DIMMAT-CM_S2013/MIT-2775 project.

Acknowledgments: The work presented here is done within the Joint Programme on Nuclear Materials of the European Energy Research Alliance Pilot Project CREMAR.

Conflicts of Interest: The authors declare no conflict of interest.

References

1. Dahl, W. *Steel: A Handbook for Materials Research and Engineering*; Springer: Berlin, Germany; New York, NY, USA; Verlag Stahleisen: Düsseldorf, Germany, 1992.
2. Morrison, W.B. Influence of testing direction on the mechanical properties of wrought steel. *Met. Technol.* **1975**, *2*, 33–41. [[CrossRef](#)]
3. Larson, F.; Zarkades, A. *Properties of Textural Titanium Alloys*; Batelle Columbus Laboratories: Columbus, OH, USA, 1974.
4. Chao, J.; Capdevila, C. Anisotropy in mechanical properties and fracture behavior of an oxide dispersion Fe₂₀Cr₅Al alloy. *Metall. Mater. Trans. A* **2014**, *45*, 3767–3780. [[CrossRef](#)]
5. Kasada, R.; Lee, S.G.; Isselin, J.; Lee, J.H.; Omura, T.; Kimura, A.; Okuda, T.; Inoue, M.; Ukai, S.; Ohnuki, S.; et al. Anisotropy in tensile and ductile–brittle transition behavior of ODS ferritic steels. *J. Nucl. Mater.* **2011**, *417*, 180–184. [[CrossRef](#)]
6. Hosford, W.F.; Backofen, W.A. *Strength and Plasticity of Textured Metals in Fundamentals of Deformation Processing*; Syracuse University Press: Syracuse, NY, USA, 1964.
7. Allen, N.P.; Earley, C.C.; Hale, K.F.; Rendall, J.H. Fracture of cold-worked iron. *J. Iron Steel Inst.* **1964**, *202*, 808.
8. Echeverria, A.; Linaza, M.A.; Rodriguez-Ibabe, J.M. Cleavage Fracture Micromechanisms in Ti, Ti-V and C-Mn-B Microalloyed Bainitic Steels. In Proceedings of the International Conference on Microalloying in Steels, Donostia-San Sebastian, Spain, 7–9 September 1998; Rodriguez-Ibabe, J.M., Gutierrez, I., Lopez, B., Eds.; Trans Tech Publications Ltd.: Zuerich, Switzerland, 1998; Volume 284, pp. 351–358.
9. Echeverria, A.; Rodriguez-Ibabe, J. Brittle fracture micromechanisms in bainitic microalloyed steels. *Int. J. Fract.* **1998**, *89*, L39–L44.
10. Inagaki, H.; Kurihara, K.; Kozasu, I. Influence of crystallographic texture on strength and toughness of control-rolled high-tensile strength steel. *Trans. Iron Steel Inst. Jpn.* **1977**, *17*, 75–81. [[CrossRef](#)]

11. Koh, B.H.J.; Kwa, C.A.; Manoharan, M. Mixed-mode impact behaviour of a low carbon steel. *Int. J. Fract.* **1996**, *77*, R77–R81. [[CrossRef](#)]
12. Chao, J.; Aranda, M.M.; Rementeria, R.; Serrano, M.; Capdevila, C. On the anisotropy of the ductile to Brittle Transition behavior in a wrought and in two oxide dispersion strengthened FeCrAl steels. *Metall. Mater. Trans. A Phys. Metall. Mater. Sci.* **2019**, *50A*, 625–640. [[CrossRef](#)]
13. Chao, J.; Rementeria, R.; Aranda, M.; Capdevila, C.; Gonzalez-Carrasco, J.L. Comparison of ductile-to-Brittle Transition behavior in two similar ferritic oxide dispersion strengthened alloys. *Materials* **2016**, *9*, 637. [[CrossRef](#)]
14. Chao, J.; Cristina, M.C.; Gonzalez-Carrasco, J.L.; Gonzalez-Doncel, G. Effect of the thermomechanical processing on the mechanical properties of MA 956 alloy. In *Materials for Advanced Power Engineering*; Lecomte-Beckers, J., Carton, M., Schubert, F., Ennis, P.J., Eds.; Forschungszentrum Jülich GmbH: Jülich, Germany, 1998; Volume 2, pp. 827–833.
15. Hupalova, M.F.; Terada, M.; Kliauga, A.M.; Padilha, A.F. Microstructural characterization of INCOLOY alloy MA 956. *Materialwiss. Werkstofftech.* **2003**, *34*, 505–508. [[CrossRef](#)]
16. Czyrskafilonowicz, A.; Wrobel, M.; Dubiel, B.; Ennis, P.J. Transmission electron-microscopy study of dislocation-dispersoid interaction in deformed incoloy ma956. *Scr. Metall. Mater.* **1995**, *32*, 331–335. [[CrossRef](#)]
17. Garfinkle, M.; Garlick, R.G. A stereographic representation of knoop hardness anisotropy. *Trans. Metall. Soc. AIME* **1968**, *242*, 809.
18. Masumoto, H.; Kikuchi, M. Elastic anisotropy and its temperature dependence of single crystals of fe-19.43 percent cr alloy. *Trans. Jpn. Inst. Met.* **1971**, *12*, 90. [[CrossRef](#)]
19. Chao, J.; Gonzalez-Carrasco, J.L. Influencia del procesado de la aleación MA956 sobre la temperatura de transición dúctil-frágil. In *VIII Congreso Nacional de Propiedades Mecánicas de Sólidos*; Amigó, V., Ed.; Universidad Politécnica de Valencia: Gandia, Spain, 2002; pp. 385–390.
20. Danniels, F.W.; Dunn, G.C. The effect of orientation on Knoop hardness on single crystals of zinc and silicon ferrite. *Trans. Am. Soc. Met.* **1949**, *41*, 419–442.
21. Lim, Y.Y.; Chaudhri, M.M. The influence of grain size on the indentation hardness of high-purity copper and aluminium. *Philos. Mag. A* **2002**, *82*, 2071–2080. [[CrossRef](#)]
22. Schmid, E.; Boas, W. *Plasticity of Crystals, with Special Reference to Metals*; Chapman & Hall: London, UK, 1968.
23. Hosford, W.F. *The Mechanics of Crystals and Textured Polycrystals*; Oxford University Press: New York, NY, USA, 1993.
24. Houtte, V. *Some Recent Developments in the Theories for Deformation Texture Prediction*; Netherlands Soc for Materials Science: Zwijndrecht, The Netherlands, 1984; pp. 7–23.
25. Noble, F.W.; Hull, D. Deformation of single crystals of iron 3% Silicon. *Philos. Mag.* **1965**, *12*, 777–796. [[CrossRef](#)]
26. Busby, J.T.; Hash, M.C.; Was, G.S. The relationship between hardness and yield stress in irradiated austenitic and ferritic steels. *J. Nucl. Mater.* **2005**, *336*, 267–278. [[CrossRef](#)]
27. Higgy, H.R.; Hammad, F.H. Effect of fast-neutron irradiation on mechanical-properties of stainless-steels—aisi types 304, 316 and 347. *J. Nucl. Mater.* **1975**, *55*, 177–186. [[CrossRef](#)]
28. Lai, M.O.; Lim, K.B. On the prediction of tensile properties from hardness tests. *J. Mater. Sci.* **1991**, *26*, 2031–2036. [[CrossRef](#)]
29. Pavlina, E.J.; Van Tyne, C.J. Correlation of yield strength and tensile strength with hardness for steels. *J. Mater. Eng. Perform.* **2008**, *17*, 888–893. [[CrossRef](#)]
30. Ishlinsky, A.J. Some applications of statistics in describing deformation laws. *Acad. Sci. USSR* **1944**, *45*, 179–180.
31. British, S.I. *Fracture Mechanics Toughness Tests Part 2: Method for Determination of K_{Ic}, Critical CTOD and Critical J Values of Welds in Metallic Materials*; British Standard Institution: London, UK, 1997; Volume BS 7448-2.
32. Sohncke, L. Über die Cohäsion des Steinsalzes in krystallographisch verschiedenen Richtungen. *Ann. Phys. Chem.* **1869**, *17*, 177–200. [[CrossRef](#)]
33. Hahn, G.T. The influence of microstructure on brittle-fracture toughness. *Metall. Trans. A* **1984**, *15*, 947–959. [[CrossRef](#)]
34. McMahon, C.J.; Cohen, M. Initiation of cleavage in polycrystalline iron. *Acta Metall.* **1965**, *13*, 591. [[CrossRef](#)]

35. Rodriguez-Ibabe, J.M. The role of microstructure in toughness behaviour of microalloyed steels. In *Proceedings of the International Conference on Microalloying in Steels*; RodriguezIbabe, J.M., Gutierrez, I., Lopez, B., Eds.; Trans Tech Publications Ltd.: Zuerich, Switzerland, 1998; Volume 284, pp. 51–62.
36. Griffith, A.A., VI. The phenomena of rupture and flow in solids. In *Philosophical Transactions of the Royal Society of London. Series A, Containing Papers of a Mathematical or Physical Character*; Royal Society: London, UK, 1921; Volume 221, pp. 163–198.
37. Irwin, G.R. Fracture. In *Elasticity and Plasticity/Elastizität und Plastizität*; Flügge, S., Ed.; Springer: Berlin/Heidelberg, Germany, 1958; pp. 551–590. [[CrossRef](#)]
38. Tada, H.; Paris, P.C.; Irwin, G.R. *The Stress Analysis of Cracks Handbook*; Paris Productions & (Del Research Corp.): Saint Louis, MO, USA, 1985.
39. Bilby, B.A.; Cardew, G.E.; Howard, I.C. Stress intensity factors at the tips of kinked and forked cracks. In *Analysis and Mechanics*; Taplin, D.M.R., Ed.; Pergamon: Oxford, UK, 1978; pp. 197–200. [[CrossRef](#)]
40. Cotterell, B.; Rice, J. Slightly curved or kinked cracks. *Int. J. Fract.* **1980**, *16*, 155–169. [[CrossRef](#)]
41. Baczynski, G.J.; Jonas, J.J.; Collins, L.E. The influence of rolling practice on notch toughness and texture development in high-strength linepipe. *Metall. Mater. Trans. A* **1999**, *30*, 3045–3054. [[CrossRef](#)]
42. Ju, J.B.; Lee, J.S.; Jang, J.I. Fracture toughness anisotropy in a API steel line-pipe. *Mater. Lett.* **2007**, *61*, 5178–5180. [[CrossRef](#)]



© 2020 by the authors. Licensee MDPI, Basel, Switzerland. This article is an open access article distributed under the terms and conditions of the Creative Commons Attribution (CC BY) license (<http://creativecommons.org/licenses/by/4.0/>).